Research Square

Preprints are preliminary reports that have not undergone peer review.
They should not be considered conclusive, used to inform clinical practice,
or referenced by the media as validated information.

Fabrication and Optimization of M2 High-Speed Steel via PBF–LB/M: A Machine Learning-Driven Approach

Sumit Sahu

sumit.kumar.sahu@iehk.rwth-aachen.de

RWTH Aachen University

Anish Upadhyaya

Indian Institute of Technology Kanpur

Felix Oppermann

RWTH Aachen University

Ulrich Krupp

RWTH Aachen University

Research Article

Keywords: M2 high-speed steel, PBF–LB/M, Machine learning, Data-driven approach, Hatch spacing, Microstructure, Crystallographic texture

Posted Date: September 9th, 2026

DOI: https://doi.org/10.21203/rs.3.rs-10818108/v1

License: This work is licensed under a Creative Commons Attribution 4.0 International License.
Read Full License

Additional Declarations: No competing interests reported.

Fabrication and Optimization of M2 High-Speed Steel via PBF–LB/M: A Machine Learning-Driven Approach

Abstract

M2 high-speed steel (HSS) exhibits high hardness and wear resistance, but its high carbon and alloy contents make crack-free fabrication by laser-based powder bed fusion (PBF–LB/M) challenging. This study develops a data-driven strategy for processing M2 HSS without preheating the baseplate. An initial dataset of 27 experiments varying laser power, scanning speed, and hatch spacing was used to predict hardness and relative density using five machine-learning algorithms and quadratic response surface modelling. Model optimization and evaluation were performed using repeated nested cross-validation. Random Forest achieved the highest predictive performance for hardness ($R2 = 0.592 \pm 0.078$), while Gradient Boosting Regression performed best for relative density ($R2 = 0.619 \pm 0.048$). Sensitivity analysis identified hatch spacing as the dominant processing parameter. Consequently, hatch spacings of 55–70 µm were explored computationally, and 60 µm was selected for experimental verification. This condition produced a relative density of 99.94 – 99.99 % and an HV hardness of 718–782, while suppressing the delamination observed at larger hatch spacings by increasing melt-track overlap and improving consolidation. Microstructural characterization revealed a refined non-equilibrium structure containing approximately 50.3% retained austenite and 24% bcc phase, with an average grain size of ~0.8 µm. Electron backscatter diffraction revealed a strong crystallographic texture (10.21 MRD) tilted 31.3° from the build direction toward [101]. These results demonstrate that data-driven parameter selection, combined with experimental verification, provides an effective strategy for improving the processability of crack-sensitive M2 HSS via PBF–LB/M.

Keywords: M2 high-speed steel; PBF–LB/M; Machine learning; Data-driven approach; Hatch spacing; Microstructure; Crystallographic texture

1. Introduction

M2 high-speed steel (HSS) is a tungsten-molybdenum with exceptional balanced mechanical properties, i.e. red hardness, high strength, wear resistance, and tempering stability [1,2]. However, the production of these high-carbon, high-alloy steels via methods such as casting [3–6] or traditional powder metallurgy [7,8] often results in coarse primary eutectic carbides, and elemental segregation during slow solidification leads to non-uniform mechanical properties. In contrast, additive manufacturing (AM) is the most promising method for fabricating HSS because it enables rapid cooling, thereby inhibiting compositional segregation and enhancing mechanical properties [9–13]. It also supports complex geometry with near-net-shape, reducing material waste. Even though segregation can be somewhat reduced using conventional powder metallurgy methods, several issues remain, including lengthy processing routes, limitations on fabricating complex components, high production costs, and long lead times. [8].

Recent advances in various AM methods for printing HSSs, including material jetting (MJ) [14–16], direct energy deposition (DED) [17–20], and powder bed fusion (PBF) [21–23], have yielded better carbide morphology and mechanical properties than those achieved with conventional routes. Rapid cooling promotes the formation of finely dispersed carbide precipitates, thereby significantly enhancing mechanical properties [24,25]. Laser powder bed fusion (PBF – LB/M) exhibits the highest cooling rate among AM methods, typically ranging from 10^3 to 10^6 K/s, leading to rapid solidification. This non-equilibrium solidification prevents full diffusion of the alloying elements, resulting in microsegregation and a fine, metastable carbide distribution [26–29]. HSS's high carbon content and rich alloying composition promote the formation of hard, brittle martensite and carbide precipitates during fast solidification in PBF-LB/M [30,31]. These microstructural characteristics, along with steep temperature gradients and thermal cycling, lead to significant residual stresses that initiate and propagate cracks, resulting in delamination [32,33]. Baseplate preheating is frequently used to reduce thermal stresses by lowering cooling rates and temperature gradients; however, it introduces new issues, such as increased process complexity, increased energy consumption, and potential changes in microstructure and phase balance [34]. Therefore, producing defect-free HSS without preheating remains challenging because many interrelated process parameters are involved, and extensive trial-and-error is required to mitigate crack formation in PBF–LB/M. Because of this, using traditional experimental approaches alone renders discovering the defect-free process expensive, time-consuming, and ineffective. In recent years, to reduce the

number of experiments, a data-driven approach has been incorporated into the experiment. Simson et al. [34] examined the effect of the PBF-LB/M parameter on single-track morphology and geometry and successfully developed a neural network (NN) model to predict single-track geometric characteristics using 30 data points. Galarza et al. [35] successfully predicted defect pores using different ML models with 18 samples. Chernyavsky et al. [36] used only 5 data points to address cracks and porosity in the AA2024 alloy. A data-driven approach can solve problems with a limited number of data points when applied correctly.

The aim of this study was to discover stable PBF-LB/M processing of M2 HSS without baseplate preheating using a data-driven approach. Relative density and hardness were considered the target responses, and an initial experimental dataset was created by systematically varying laser power, scanning speed, and hatch spacing. To determine trustworthy process-property correlations, five supervised machine-learning methods and a traditional quadratic response-surface model were assessed using a repeated nested cross-validation framework. To identify a promising processing condition for experimental verification, the most influential parameter was further investigated over an extended parameter range after the relative influence of the key processing parameters was evaluated through sensitivity analysis. In order to determine the connections between processing conditions, microstructural evolution, phase constitution, and crystallographic features, the final material was further characterized. In the PBF-LB/M processing of crack-sensitive M2 HSS without baseplate preheating, this study offers an integrated, data-driven experimental framework to guide parameter selection and elucidate process–structure–property interactions.

2. Materials and methodology

2.1 Material

Pre-alloyed M2 tool steel powder was purchased from GKN Hoeganaes, Buzau, Romania, specifically produced for PBF-LB/M applications. According to the supplier data, the apparent density (Hall) and tap density of the powder are respectively 4.30 g/cm^3 and 5.40 g/cm^3, while the theoretical density is 8.1 g/cm^3. The particle size distribution (PSD), characterised by the D10, D50, and D90 values, is 17 μm, 31 μm, and 53 μm, respectively, as determined by sieve analysis. The detailed chemical composition of M2 HSS, as provided by the supplier, is given in Table 1.

Table 1. Chemical analysis of M2 HSS powders (wt%)

C	Mo	W	V	Cr	Ni	Co	Si	Mn	Fe

0.89	4.78	6.06	2.02	4.11	0.2	0.02	0.32	0.36	Bal.

2.2 Laser powder bed fusion processing

For PBF-LB/M, an AconityMini printer (Aconity 3D, Herzogenrath, Germany) was used in this experiment. It featured a 400 W fibre laser system with baseplate preheating up to 800 °C. Without baseplate preheating, all PBF-LB/M samples were printed on 304L stainless steel substrate plates with an 80 μm laser spot size. The powder was first dried in the vacuum drying oven VT 6025 for 12 hours at 100ºC. Afterwards, the powder was fed into the AconityMini chamber. To reduce the potential of oxidation, the chamber was continuously purged with argon gas, keeping the oxygen content low (below 500 ppm). The scanning direction of each layer was rotated by 90° relative to the preceding layer, with a layer thickness (t) of 30 μm. A meander-scanning approach with skywriting was employed. In the first print, 27 samples of the 5mm × 5mm × 10 mm specifications were produced by varying laser power (P), hatch distance (h), and scanning speed (v).

Table 1 PBF-LB/M parameters for initial printing

Parameters	1	2	3
Laser Power (W)	180	200	220
Scanning Speed (mm/s)	800	1000	1200
Hatch spacing (μm)	80	100	120

The initial print aims to provide training data to develop a machine learning model that identifies the stable processing window for M2 HSS and determines correlations between process parameters and relative density and bulk hardness.

2.3 Machine Learning

The initial model-development dataset included 27 LPBF trials at three laser powers (180, 200, and 220 W), scanning speeds (800, 1000, and 1200 mm/s), and hatch spacings (80, 100, and 120 μm). Hardness and relative density were treated separately as the two target responses. Layer thickness was kept constant at 30 μm throughout all tests, it was not included as an independent model input. A constant variable does not provide statistical information for determining its influence.

The primary feature set included the separately configurable LPBF parameters:

$$X = [P, v, h] \quad (1)$$

where P, v, and h represent the laser power, scanning speed, and hatch spacing, respectively. Volumetric energy density (VED), linear energy density (LED), and a Rosenthal-type

parameter (R_f) were further assessed to see if physically derived representations of the processing parameters enhanced prediction:

$$VED = \frac{P}{v.h.t} \quad (2)$$

$$LED = \frac{P}{v} \quad (3)$$

$$R_f = \frac{P}{\sqrt{v}} \quad (4)$$

Thus, three feature sets were evaluated: (i) the key parameters P, v, and h; (ii) the three derived descriptors; and (iii) a combined six-variable feature set. Rather than being treated as independent experimental variables, the resulting descriptors were assessed using feature-ablation analysis, as they represent deterministic changes in the core processing variables.

Five machine-learning algorithms—Bayesian Ridge regression, Random Forest (RF), Gradient Boosting Regression (GBR), Support Vector Regression (SVR), and Gaussian Process Regression (GPR)—were compared to a standard quadratic response surface model (RSM). A repeated layered cross-validation architecture was used to decouple hyperparameter tuning from performance evaluation, reducing data leakage and overestimation of performance. To examine model robustness, we also used feature-ablation, Y-randomization, learning-curve analysis, leave-one-hatch-spacing-out validation, and cross-validated permutation importance. Bayesian Ridge Regression depicts regression coefficients probabilistically and incorporates regularization via prior distributions. In particular, Gaussian priors used for the regression coefficients cause shrinkage similar to the (L_2) regularization used in traditional ridge regression. This regularization reduces overly large coefficient estimates and enhances the model's stability in the presence of limited data, noise, and correlated predictor variables. [37–39].

Gaussian Process Regression (GPR) is a non-parametric Bayesian framework that defines the target response surface as a collection of random variables with a joint Gaussian distribution. Its covariance structure is determined by a Kernel function, which can be expressed as the Radial Basis Function (RBF) [40–43] as given by

$K(x, x') = \sigma_f^2 \exp(-\frac{\|x-x'\|^2}{2l^2})$, where l represents the characteristic length scale (5)

This enables the model to provide a formal measure of predictive uncertainty in addition to a mean prediction by quantifying the statistical similarity between coordinates in the input feature space. Support Vector Regression (SVR) was used to map high-dimensional non-linearities. A regression function that maintains a maximum deviation of $\in$ from the real goals is given by

$$f(x) = \{w, \phi(x)\} + b \quad (6)$$

This is accomplished by using a hinge loss function and a regularization constant, which strikes a balance between model flatness and training accuracy, to solve a dual optimization problem that minimizes the weight vector norm $\| w \|^2$, while penalizing errors beyond the $\in$-tube [44,45].

To capture complex, non-linear interaction effects among process factors, decision tree-based ensemble models were investigated. Random Forest (RF) uses bootstrap aggregation (bagging) to minimize model variance. It generates many decision trees during training and yields an average prediction, effectively decorrelating the trees by selecting a random subset of features at each split [40]. Gradient Boosting (GBR) is a sequential additive method to reduce a loss function (usually Mean Squared Error) via gradient descent. Each consecutive tree is trained to forecast the previous ensemble's residuals (errors), allowing the model to focus on the most difficult-to-predict portions of the parameter space [47,48]. Ridge Regression offered a linear baseline that was regularized. To reduce the coefficients of less significant features and avoid over-fitting, it employs an L_2 penalty term, which is added to the sum of squared residuals as $\sum \lambda \| w \|^2$ [49,50].

In addition to machine-learning models, a traditional quadratic Response Surface Methodology (RSM) model was used as a benchmark to assess predictive performance. The second-order polynomial model includes linear, quadratic, and two-factor interaction factors, allowing for the depiction of curvature and interactions between process parameters [51,52]. The response was expressed as:

$$y = \beta_0 + \beta_1 P + \beta_2 v + \beta_3 h + \beta_{11} P^2 + \beta_{22} v^2 + \beta_{33} h^2 + \beta_{12} Pv + \beta_{13} Ph + \beta_{23} vh \quad (7)$$

The addition of the RSM enabled the practical predictive advantage of the ML approaches to be examined relative to a standard factorial-analysis framework, thus addressing the criticism that the benefits of ML should not be assumed solely on the basis of model complexity.

Prior to establishing process-property correlations and making subsequent predictions, each regression algorithm underwent rigorous hyperparameter optimization utilizing a repeated nested cross-validation framework. This strategy was chosen to reduce overfitting and prevent information leakage between model tuning and performance evaluation, which is especially relevant given the limited experimental dataset used in the current investigation. The nested technique included an exterior five-fold cross-validation that was performed five times to estimate model generalization unbiasedly, as well as an inner three-fold cross-validation for hyperparameter optimization. The dataset was split into training and validation subsets at each

outer iteration, and hyperparameter selection was limited to the training subset via a grid search within the inner cross-validation loop. The top-performing model was then assessed on the relevant outer validation fold, which remained hidden during model tuning. The model's performance was provided as the mean ± standard deviation of the cross-validated coefficient of determination (R^2), mean absolute error (MAE), and root mean square error (RMSE). The five machine-learning algorithms: Bayesian Ridge, Random Forest, Gradient Boosting Regression, Support Vector Regression, and Gaussian Process Regression, as well as the standard quadratic response-surface model, were all validated using the same technique. To compare model performance, we used R^2, MAE, and RMSE rather than a single train-test split. Following model creation, cross-validated permutation importance was used to identify the most relevant processing parameter, and the resulting sensitivity analysis guided subsequent investigation into reduced hatch spacing.

2.3 Characterisation of powder

Revolution Powder Analyser (RPA) (Mercury Scientific Inc., Newtown, CT, USA) was used to study the flowability and adhesion of M2 HSS powder. Contrast-based photos of the avalanching powder surface were taken during the experiment in a horizontally rotating drum, and the rheological characteristics (e.g., avalanche angle, flow factor, cohesion, break energy, etc.) of the powder were examined. CAMSIZER X2 (Microtrac Retsch GmbH) was used to investigate particle size distribution and morphology; the results for relative and cumulative frequency are shown in Fig. 1a. Sphericity, symmetry, and b/l3 values are 0.806, 0.947, and 0.891, respectively, indicating high sphericity and an ideal aspect ratio for 3D printing, as they maximise flowability and packing density. Scanning electron microscopy (SEM) at IEHK (FEG Zeiss Sigma) was used to analyse the microstructure and verify the particle's sphericity, as shown in Fig. 1b.

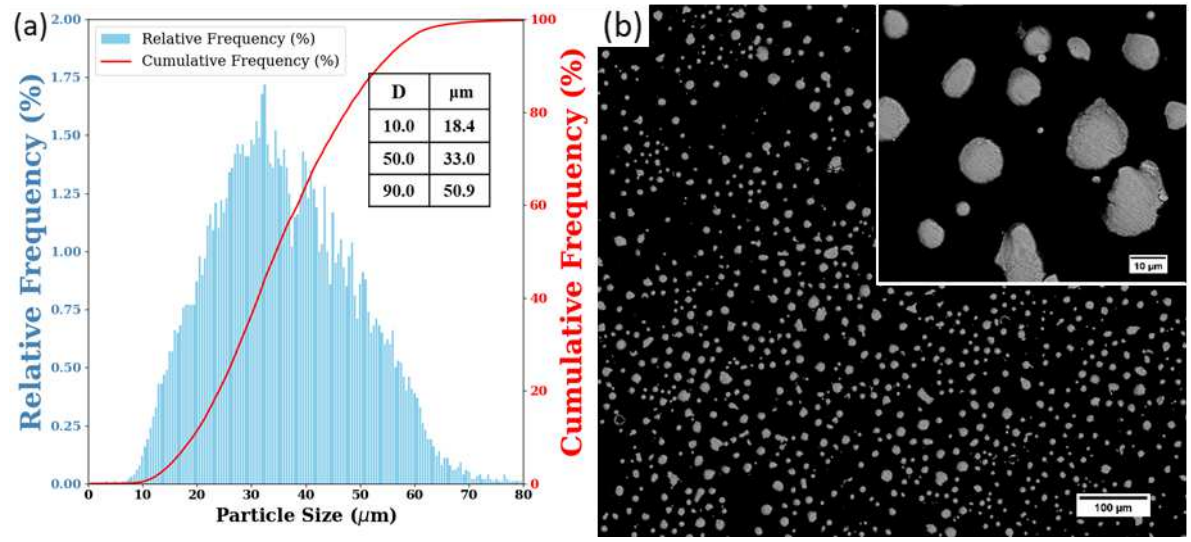


Fig. 1 (a) Particle size distribution and (b) BSE image of M2 high-speed steel powder

2.4 Characterisation of printed sample

To examine the microstructure, optical microscopy (OM) and SEM are used. For the printed sample preparation, it was first hot-mounted, then mechanically ground using silicon carbide paper, starting with progressively finer grits (80 to 2000 grit), with water lubrication. Then it was moved to cloth polishing, where colloidal silica (6 µm, 3 µm, and 1µm) is used. Fiji software is used to calculate the relative density of the printed sample from the OM image using area fraction. To determine the average relative density, five images are acquired from each sample at different locations. A back-scattered electron (BSE) image was captured at 20 kV and a working distance of 8-12 mm, and used to analyse the morphology of the melt pool and to track the evolution of the microstructure. Additionally, energy-dispersive X-ray spectroscopy (EDS) is used alongside SEM to map alloy segregation (W, Mo, and V) and monitor elemental homogeneity in printed parts. For electron backscatter diffraction (EBSD), cloth-polished samples were polished in Vibromet for 16 hours in 0.06 µm silica suspension, and Oxford's EBSD detector with AztecCrystal software was used to capture the data. The EBSD data were then analysed in MATLAB 2024 using the MTEX 6.1.0 toolbox.

Bulk hardness testing was conducted at room temperature using a load of 30 kgf in the Hardness Tester for Vickers and Brinell (Dia Tester 731). For the Vickers hardness test, a regular four-sided diamond pyramid with a face angle of 136° is used. Ten indents were taken from each sample, in the middle and along the build direction.

3. Results and discussion

3.1 Initial laser powder bed fusion printing

PBF-LB/M has up to 12 important input process parameters that affect the microstructure and mechanical properties of the printed sample, thereby increasing the number of possible combinations to print and further increasing the time and cost required to determine a stable set of parameters [53,54]. Thus, the three parameters, laser power, scanning speed and hatch spacing, are varied in the initial printing. Samples of size 5mm × 5mm × 10 mm with a V-shape at the bottom were printed in 27 different combinations of laser power, scanning speed and hatch distance while other parameters were kept constant (Fig. 2a). However, due to a high amount of alloying elements and carbon content, the rapid solidification during PBF-LB/M promotes the formation of hard and brittle martensite with carbides. When combined with a steep thermal gradient and high internal stresses, it leads to crack initiation, propagation, and eventually delamination in the component (Fig. 2a) [31,55–57]. OM micrographs with different hatch spacings in the build direction (BD) are shown in Fig. 2b, Fig. 2c, and Fig. 2d. The experimental results show that the relative density decreases slightly as the hatch spacing increases. At a hatch spacing of 80 µm, the average relative density (average of 9 samples printed with the same hatch spacing) is ~99.87 %. This reduced to ~99.75% at 100 µm and ~99.68% at 120 µm across nine parameter combinations with varying laser strengths and scanning rates (Table 2). Similarly, average bulk hardness decreased from ~725 HV at 80 µm to ~678 HV at 100 µm and ~673 HV at 120 µm, with a maximum hardness of 754 HV at 180 W and 800 mm/s (Table 2). The higher densification and hardness at lower hatch spacing might be due to greater overlap between adjacent melt tracks, which improved metallurgical bonding, promoted uniform energy distribution, and reduced lack-of-fusion flaws.

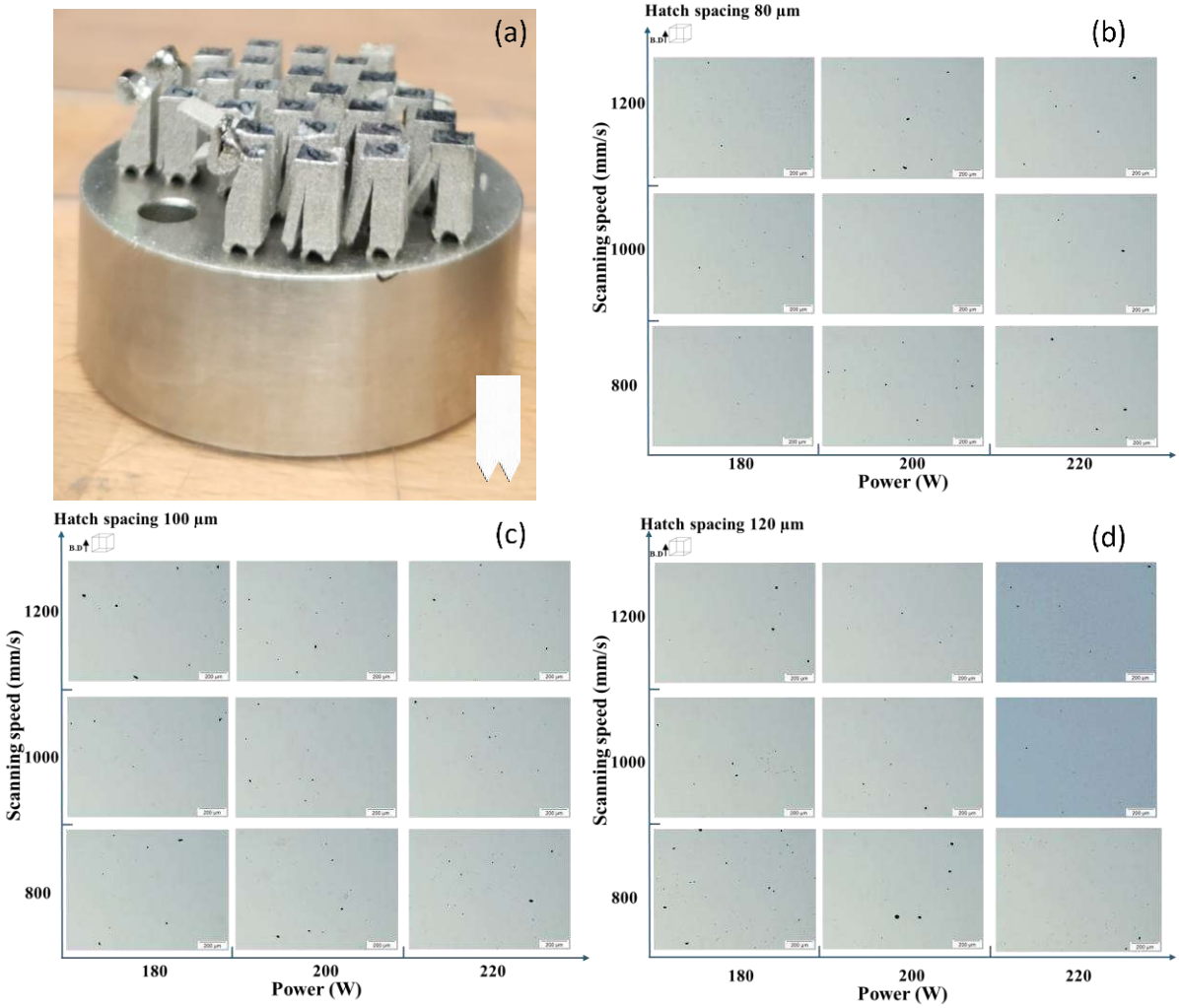


Fig. 2 Printed samples with initial parameters (a), and optical microscopy micrographs with respect to hatch spacing (b) 80 µm, (c) 100 µm, (b) 120 µm

Table 2 PBF-LB/M parameters, relative density, bulk hardness and VED

Laser power (W)	Scanning speed (mm/s)	Hatch spacing (µm)	VED (J/mm^3)	Hardness (HV)	Relative density OM (%)
180	800	80	93.75	754.40 ± 25.18	99.92 ± 0.04
180	1000	80	75.00	721.10 ± 06.21	99.86 ± 0.02
180	1200	80	62.50	727.50 ± 19.12	99.88 ± 0.05
200	800	80	104.17	743.10 ± 14.46	99.87 ± 0.03
200	1000	80	83.33	737.00 ± 20.49	99.88 ± 0.03
200	1200	80	69.44	700.50 ± 14.49	99.82 ± 0.08
220	800	80	114.58	720.90 ± 20.42	99.89 ± 0.06
220	1000	80	91.67	710.00 ± 07.29	99.85 ± 0.03
220	1200	80	76.39	713.50 ± 14.18	99.86 ± 0.05
180	800	100	75.00	673.90 ± 08.75	99.77 ± 0.02
180	1000	100	60.00	687.70 ± 27.68	99.72 ± 0.04
180	1200	100	50.00	685.70 ± 13.13	99.74 ± 0.11

200	800	100	83.33	681.40 ± 19.31	99.74 ± 0.09
200	1000	100	66.67	686.10 ± 17.82	99.77 ± 0.08
200	1200	100	55.56	665.60 ± 10.34	99.75 ± 0.04
220	800	100	91.67	668.70 ± 13.70	99.72 ± 0.11
220	1000	100	73.33	687.20 ± 09.64	99.79 ± 0.07
220	1200	100	61.11	670.90 ± 09.95	99.72 ± 0.03
180	800	120	62.50	687.00 ± 17.96	99.53 ± 0.12
180	1000	120	50.00	657.70 ± 09.07	99.63 ± 0.09
180	1200	120	41.67	687.50 ± 15.51	99.68 ± 0.06
200	800	120	69.44	716.00 ± 29.91	99.72 ± 0.04
200	1000	120	55.56	667.30 ± 10.39	99.74 ± 0.03
200	1200	120	46.30	665.90 ± 09.40	99.65 ± 0.02
220	800	120	76.39	657.70 ± 09.65	99.66 ± 0.01
220	1000	120	61.11	655.90 ± 17.92	99.78 ± 0.09
220	1200	120	50.93	663.20 ± 12.15	99.78 ± 0.05

3.2 Machine learning evaluation

All the data from Table 2 was fed into the five algorithms. The initial dataset consists of three input parameters (laser power, scanning speed and hatch distance) and two output parameters (hardness and relative density). For each model, a predefined hyperparameter space was provided based on regularly reported values in the literature and empirical best practices in machine learning for hyperparameter tuning [58–60], see Table 3. To ensure robust model evaluation while minimizing overfitting and information leakage, all models were subjected to a repeated nested cross-validation strategy, which included an outer five-fold cross-validation repeated five times for performance evaluation and an inner three-fold cross-validation for hyperparameter optimization.

Table 3 ML model and hyperparameter

Model	**Parameter**
Bayesian Ridge	α_1, α_2, λ_1, λ_2= [10^7,10^6,10^5,10^4]
Random forest	Trees = [200, 500]; depth = [None, 3, 5]; min. leaf = [1, 2, 3]; max. features = [1.0, √]
Support vector regression	Kernel = [RBF, linear]; C = [0.1,1,10,100]; ε = [0.01,0.05,0.10,0.20]; γ=[scale,0.01,0.10,1.0]
Gradient boosting regression	Trees = [50, 100, 200]; learning rate = [0.03, 0.05, 0.10]; depth = [1, 2, 3]; min. leaf = [1, 2, 3]; subsample = [0.7, 1.0]

Gaussian process regression	Kernel = [RBF, Matérn (ν=2.5)] with WhiteKernel; α = [10^{10},10^{6},10^{3}]; optimizer restarts = 3
Quadratic RSM	Second-order polynomial expansion + α_1, α_2, λ_1, λ_2= [10^{7},10^{6},10^{5},10^{4}]

Following hyperparameter optimization within the repeated nested cross-validation framework, the prediction capabilities of the five machine-learning algorithms and the traditional quadratic response-surface model for hardness and relative density were systematically compared. The model's performance was evaluated using the coefficient of determination (R^2), mean absolute error (MAE), and root mean square error (RMSE). Results were presented as mean ± standard deviation throughout multiple outer cross-validation cycles. Random Forest (RF) exhibited the highest predictive performance, with an R^2 of 0.592 ± 0.078 and a MAE of 14.37 ± 1.79 HV, while Gradient Boosting Regression (GBR) showed comparable performance (R^2 = 0.584 ± 0.100, MAE = 14.42 ± 2.36 HV). For relative density, GBR achieved the highest R^2 of 0.619 ± 0.048 with a MAE of 0.0438 ± 0.0032 percentage points, closely followed by RF (R^2 = 0.612 ± 0.085, MAE = 0.0445 ± 0.0050 percentage points). The conventional quadratic RSM yielded R^2 values of 0.506 ± 0.030 and 0.558 ± 0.059 for hardness and relative density, respectively, demonstrating that the ML models provided a moderate improvement over the conventional response-surface approach. Further feature-ablation investigation employing physically derived descriptors (VED, LED, and R_f) and combined features revealed that their impact varied across models; while some regression techniques exhibited gains, no consistent improvement was observed across all models. Because they reflect the independently controlled PBF-LB/M variables, the primary processing parameters were kept for further process interpretation.

Table 4 Predictive performance of regression models using primary PBF-LB/M parameters

Model	Hardness (R^2)	Hardness MAE (HV)	Density (R^2)	Density MAE (%)
Bayesian Ridge	0.522 ± 0.034	15.53 ± 0.62	0.592 ± 0.062	0.0453 ± 0.0037
Random Forest	**0.592 ± 0.078**	**14.37 ± 1.79**	0.612 ± 0.085	0.0445 ± 0.0050
Gradient Boosting	0.584 ± 0.100	14.42 ± 2.36	**0.619 ± 0.048**	**0.0438 ± 0.0032**
SVR	0.394 ± 0.147	17.74 ± 1.97	0.462 ± 0.115	0.0518 ± 0.0062
Gaussian Process	0.510 ± 0.051	15.50 ± 1.20	0.578 ± 0.122	0.0452 ± 0.0058
Quadratic RSM	0.506 ± 0.030	15.93 ± 0.57	0.558 ± 0.059	0.0474 ± 0.0036

These results show modest predictive performance rather than near-perfect prediction, as expected given the restricted experimental dataset. Nonetheless, the ensemble models reliably represented a large portion of the experimentally observed variance in hardness and relative density. The optimized models were then submitted to additional robustness tests, such as Y-randomization, learning curve evaluation, leave-one-hatch-spacing-out validation, and cross-validated permutation feature importance. The sensitivity analysis consistently identified hatch spacing as the most important processing parameter for both outcomes (Fig. 3). Rather than extrapolating across all processing parameters simultaneously, the subsequent ML-guided investigation focused solely on reducing hatch spacing to the 55-70 µm range, with 60 µm selected for experimental verification.

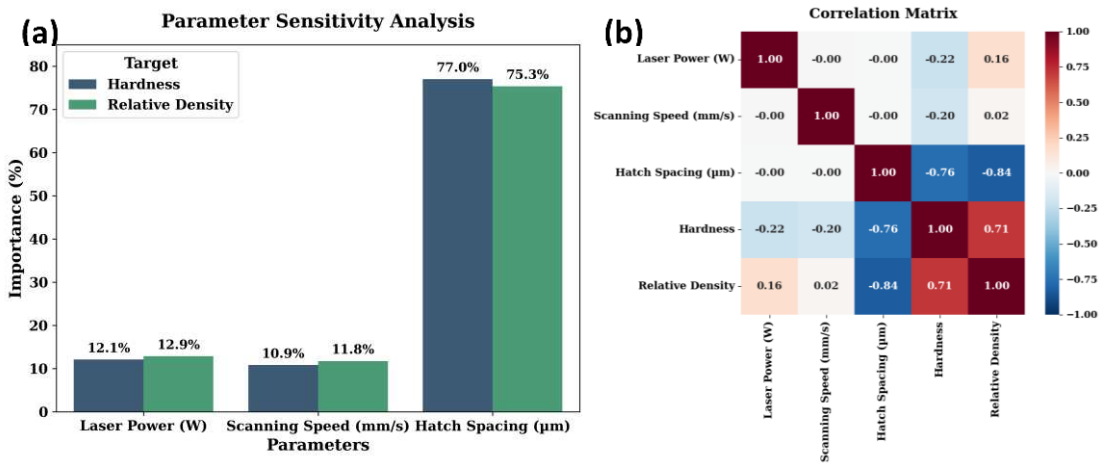


Fig. 3 Sensitivity analysis (a) and correlation matrix (b) of input and output parameters, which depicts that hatch spacing has the strongest influence

3.3 Prediction of new parameter and analysis

Based on experimental results, sensitivity analysis, and the literature [21,57,58], it was shown that hatch spacing has a greater effect on output characteristics, as selectively predicted to yield enhanced hardness and relative density when other parameters are held constant. This focused strategy makes the prediction easier by concentrating on the most sensitive variable. Moreover, it enables more efficient investigation of the process window while preserving model correctness. Based on the predicted data, a subsequent printing experiment was conducted to validate the model's results. The prediction strongly suggested a lower hatch spacing, so printing was conducted at 60 µm. Since the first sample has a V-shape at the bottom, to assess the effect of geometry on the printed sample, a 5mm × 5mm × 10 mm cuboid was printed with the best-performing parameter based on relative density and hardness, as shown in the Fig. 4a. There was also a noticeable improvement in the relative density of the printed sample (Fig. 4b), with an average of ~99.97% at a 60 µm hatch spacing compared to 80 (~99.87%), 100

(~99.75%), and 120 (~99.68%) µm. This suggests that the printed materials densified and exhibited decreased porosity. Average bulk hardness was also increased to ~746 HV (60 µm) from ~725 HV (80 µm), ~678 HV (100 µm), and ~673 HV (120 µm), showing a similar trend, with a peak at ~782 HV. The outcomes confirm that defect-free process parameters effectively improve the material's quality. More importantly, the smaller hatch spacing solved the build-integrity issue identified at greater hatch spacings. Delamination in samples manufactured at prior hatch spacings was eradicated under the 60 µm condition. Thus, the experimentally chosen setting resulted not only in high hardness and relative density but also in increased macroscopic construction integrity.

The improvement is mostly due to increasing overlap between adjacent melt tracks. Decreasing hatch spacing shortens the distance between consecutive scan vectors, allowing for more remelting of the previously consolidated track and enhancing metallurgical continuity between melt pools. Enhanced overlap lowers the likelihood of poorly bonded inter-track areas, which can serve as favorable sites for defect development and delamination.

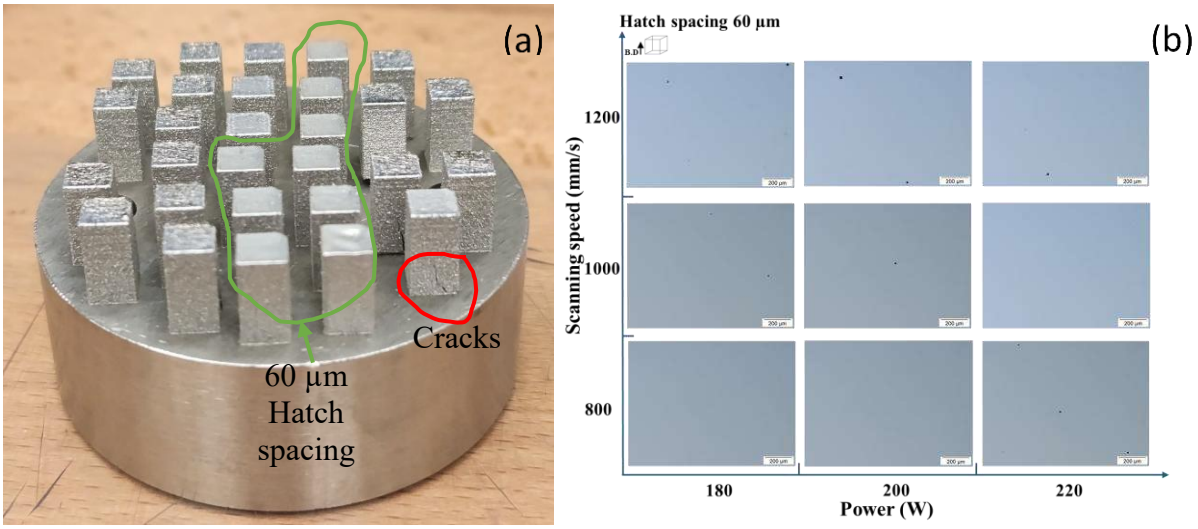


Fig. 4 Printed samples (a) with predicted parameters and previous best parameters based on higher relative density and hardness, and OM micrographs (b) with hatch spacing 60 µm

The model-predicted response maps at the ML-guided hatch spacing of 60 µm are shown in Fig. 5(a, b), which illustrates the combined effects of laser power and scanning speed on relative density and hardness, respectively. The hardness map in Fig. 5a shows that the expected reaction typically declines as laser power and scanning speed increase, with considerably higher hardness near the lower-power, lower-speed region. Similarly, at lower-to-intermediate laser powers and scanning speeds, the relative-density map in Fig. 5b predicts a high-density region; however, as laser power increases toward 220 W, the anticipated density gradually decreases. Altogether, the anticipated maps indicate that a favourable area for concurrently

achieving high hardness and relative density at 60 µm hatch spacing is roughly 180–200 W and 800–1000 mm/s.

The matching experimental results obtained after constructing samples at the chosen 60 µm hatch spacing are shown in Figure 5(c,d), allowing for direct evaluation of the model-guided parameter selection. The experimentally observed hardness shows a nonlinear dependence on laser power and scanning speed, as shown in Fig. 5(c). At 200 W and 800 mm/s, the maximum hardness of roughly 781 HV was achieved; at 180 W and 1000 mm/s, another high-hardness condition was noted (~769 HV). The hardness response cannot be adequately described by a monotonic energy-input relationship, as evidenced by the observation that increasing the scanning speed to 1200 mm/s often resulted in lower hardness, especially at 200 W. With values ranging from 99.94% to 99.99%, the experimental relative-density surface in Fig. 5(d) shows consistently strong densification across the 60 µm settings examined. The lower-to-intermediate laser-power zone produced the highest relative densities, which generally supported the favourable region shown in the anticipated response map.

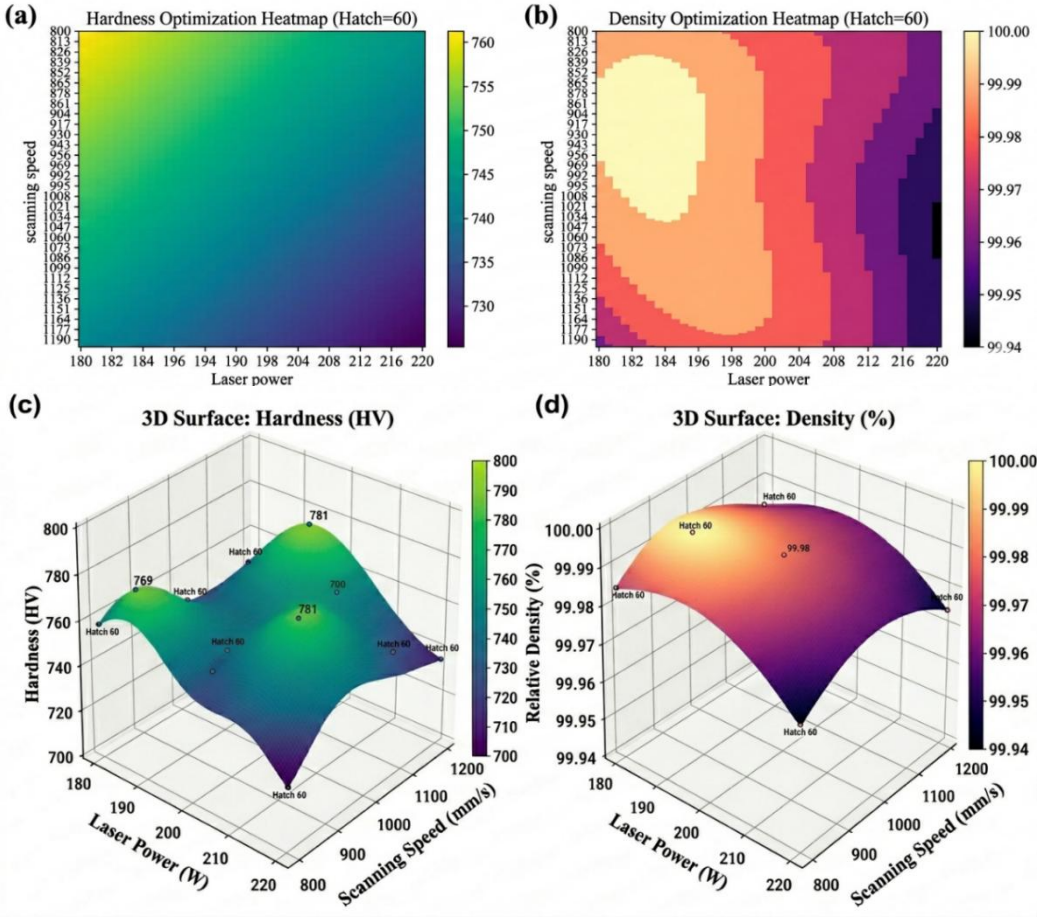


Fig. 5 ML-guided prediction and subsequent experimental verification at a hatch spacing of 60 µm: model-predicted response maps showing the combined effects of laser power and scanning speed on (a) hardness and (b) relative density; experimentally measured response surfaces showing (c) hardness and (d) relative density for samples fabricated at 60 µm hatch spacing.

Fig 6 shows the effect of hatch spacing on the hardness and relative density. Both bulk hardness and relative density increased as hatch spacing decreased. The increased lateral overlap between adjacent melt tracks, which promotes remelting and strengthens the metallurgical link between them, is the main cause of increased densification. Increased spatial overlap at a hatch spacing of 60 μm inhibits lack-of-fusion porosity and reduces inadequately melted inter-track areas, resulting in a more uniform and continuous consolidated structure. In addition to changing the local thermal history and encouraging recurrent reheating of previously hardened material, the increased remelting and thermal interaction between adjacent tracks may also aid in local stress relief. More significantly, the elimination of lack-of-fusion pores and sharp inter-track defects removes potential stress-concentration sites that could promote crack formation and propagation [30,61]. The enhancement of bulk hardness could also result from fewer microscopic lack-of-fusion (LOF) defects, and increasing overlap enables intrinsic heat treatment during processing, which aids the transformation of residual austenite into a predominantly martensitic matrix [61–63].

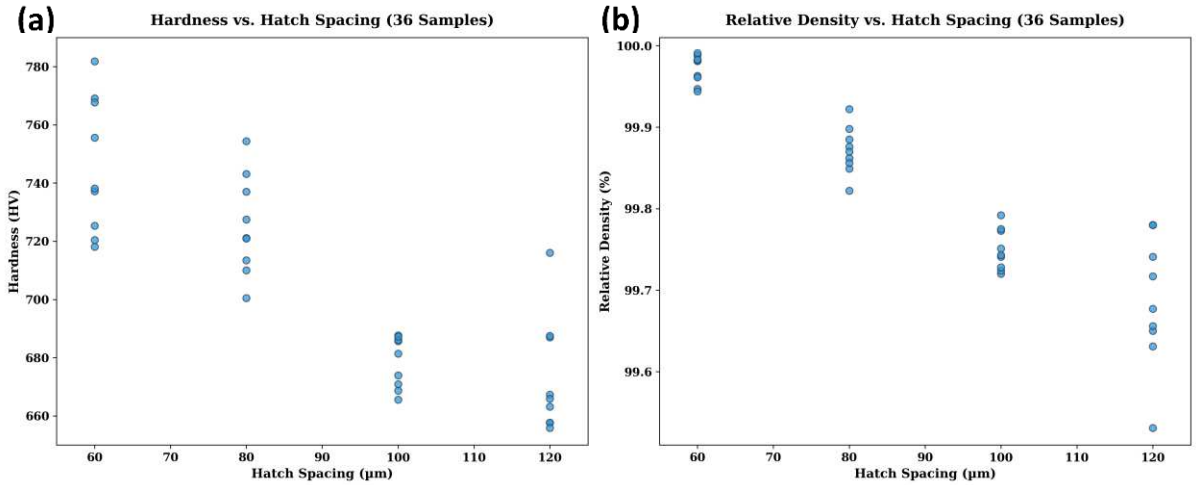


Fig. 6 Effect of hatch spacing on bulk hardness (a) and relative density (b)

3.2 Microstructural and crystallographic characterization of the printed sample

Fig. 7 shows a BSE image of the polished cross-section in the build direction. In Fig 7a, LOF, cracks, cracks with LOF, and round porosity can be easily identified in the sample printed with a 120 μm hatch spacing. LOFs are large, irregular, non-spherical voids that occur when insufficient laser energy is applied, or inappropriate hatch spacing is used, leaving unmelted or partially melted powder particles between subsequent print tracks/layers. Cracks and cracks with LOF visible as sharp micro-separations. Some are specifically linked to the LOF voids, suggesting that unbonded interfaces acted as significant stress concentrators during cyclic thermal loading, leading to solidification or thermal stress cracking. Formation of round pores

is due to the entrapment of shielding gases, such as argon, in the melt pool during rapid solidification. High cooling rates prevent trapped gas from escaping, resulting in gas-induced porosity [53]. In Fig. 7b, the shift in grain and dendritic growth morphologies across the melt-pool boundary is shown. It has been found that when the temperature gradient increases, grain growth changes from the molten pool's edges to its centre. The molten pool boundaries are primarily composed of a mix of columnar and fine equiaxed dendrites, which might have formed due to a large number of heterogeneous nucleation sites at the solid-liquid interface. The region inside the melt pool consists of a slightly coarser equiaxed structure formed due to the localized reduction of the temperature gradient [65]. A fine network of micro-segregation of the alloying element (Fig. 8b) was also observed as an equiaxed structure in Fig 7c. In Fig. 7d, columnar dendritic strains, along with secondary dendritic arms in some cases, can be easily recognised, which is the fingerprint of solidification direction [65,66]. The microstructure of the printed M2 high-speed steel is heterogeneous, with columnar and equiaxed dendritic zones. These heterogeneous microstructural characteristics indicate instability in the melt pool during solidification. During the PBF-LB/M process, temperature gradients and solidification rates fluctuate, leading to instability.

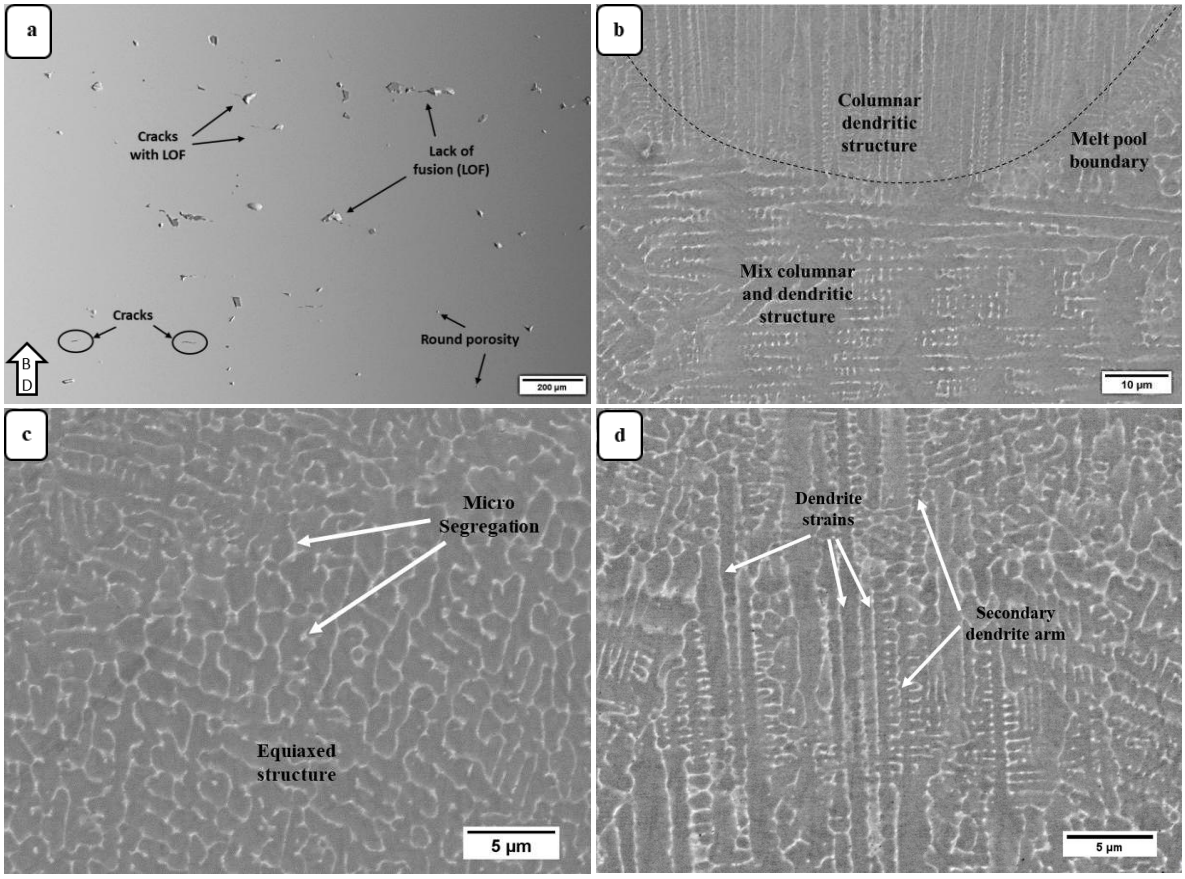


Fig. 7 BSE mode micrograph of printed sample showing (a) crack and pores, (b) melt pool boundary, (c) equiaxed structure and (d) dendrite strains in the build direction

Fig. 8 shows the EDS point scan, EDS line scan, and EDM map of M2 HSS printed with a hatch spacing of 60 µm in the build direction. In Fig. 8a, points 1 and 2 are taken in the grey region, and 3, 4, and 5 are taken in the brighter region. The grey region has higher iron content, and the brighter region has significantly more alloying elements. Fe content decreases (~15–20 %), while the content of other heavier elements (leads to bright Z contrast) increases: W (~100 %), Mo (~100 %), V (~75 %), and Cr (~40 %). An EDS line scan has been conducted, including both the grey and bright regions in Fig. 8b. The Fe signal shows a noticeable dip at approximately 4 µm, while the line of alloying elements shows a subtle upwards peak at the same location. Fig. 8c shows the EDS maps, which provide a microscopic view of the elemental distribution in printed M2 HSS. The Fe maps show a slightly darker grid pattern, indicating localised depletion along cellular boundaries, while Mo and W exhibit a clear bright skeleton structure which perfectly matches the Fe maps. This clearly demonstrates that the interdendritic walls are rich in these heavy, refractory materials. At this scale, vanadium and chromium appear generally homogeneous, while point data indicate minor segregation. Their lower atomic weight and lower partitioning coefficient make their segregation less noticeable in raw dot maps than Mo and W.

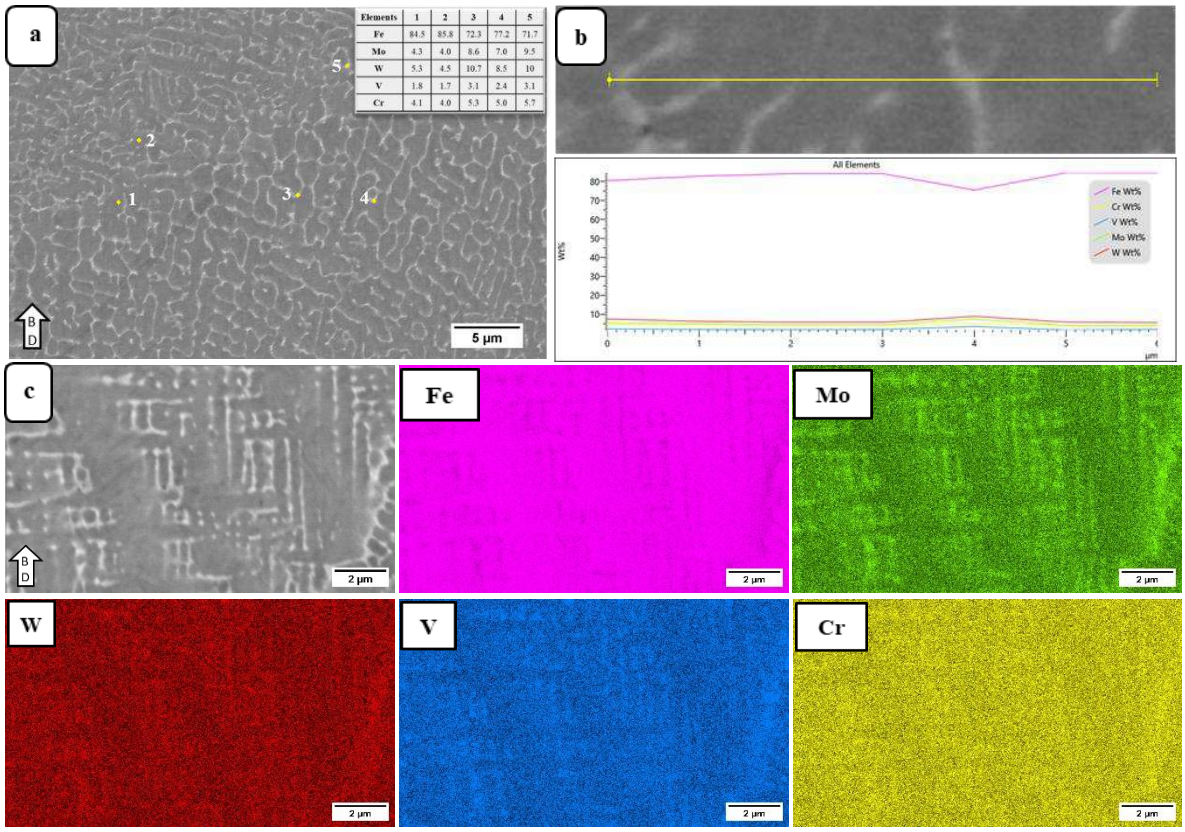


Fig. 8 EDS-point scan (a), EDS-line scan (b) and EDS-map of elements of M2 HSS printed with P = 180 W, v = 800 mm/s and h = 60 µm, indicating Fe in the grey region and Mo, W, V, Cr in the bright region

Fig. 9 shows the phase fraction map, grain shape factor map, and grain shape and size histogram for an EBSD analysis in the build direction, evaluated using the MTEX software package. Matrix is dominated by retained austenite (Iron fcc) at 50.3 %, with a refined martensite/ferrite (Iron bcc) phase at 24 % (Fig. 9a). A substantial volume fraction of retained austenite formed during rapid cooling indicated that high alloying elements (W, Mo, V, Cr, C) significantly suppressed martensite transformation by lowering the martensite start (M_s) temperature. This was further verified using Thermo-Calc software: the M_s decreases from 504.5 K to 376.1 K upon addition of the alloying elements. Although the processed and polished EBSD phase map (Fig. 9a) displays a well-refined, continuous dual-phase matrix, inspection of the raw, uncleaned EBSD data reveals that 25.7% of locations are unindexed (Zero Solutions). This might be due to a combination of ultra-fine carbide precipitation, extreme grain refinement and the high dislocation density present in rapid solidification. These unindexed spots are mostly found at lath interfaces and interlath gaps [68]. At these high-energy lath interfaces and interlath gaps, the high local dislocation density resulting from rapid solidification, together with overlapping Kikuchi patterns, might severely distort the diffraction signal, preventing effective indexation prior to the software's clean-up procedure. Fig. 9c shows the grain-size distribution histogram, which demonstrates a highly refined microstructure with the majority of grains below 2 μm and a sharp peak between 0.5 μm and 1 μm. This refinement is the primary reason for the high hardness, resulting from grain boundary strengthening (the Hall-Petch effect). Fig. 9d shows the aspect ratio histogram, indicating a predominantly columnar morphology with a peak between 2.0 and 3.0, as seen in Fig. 9b in the grain shape factor map.

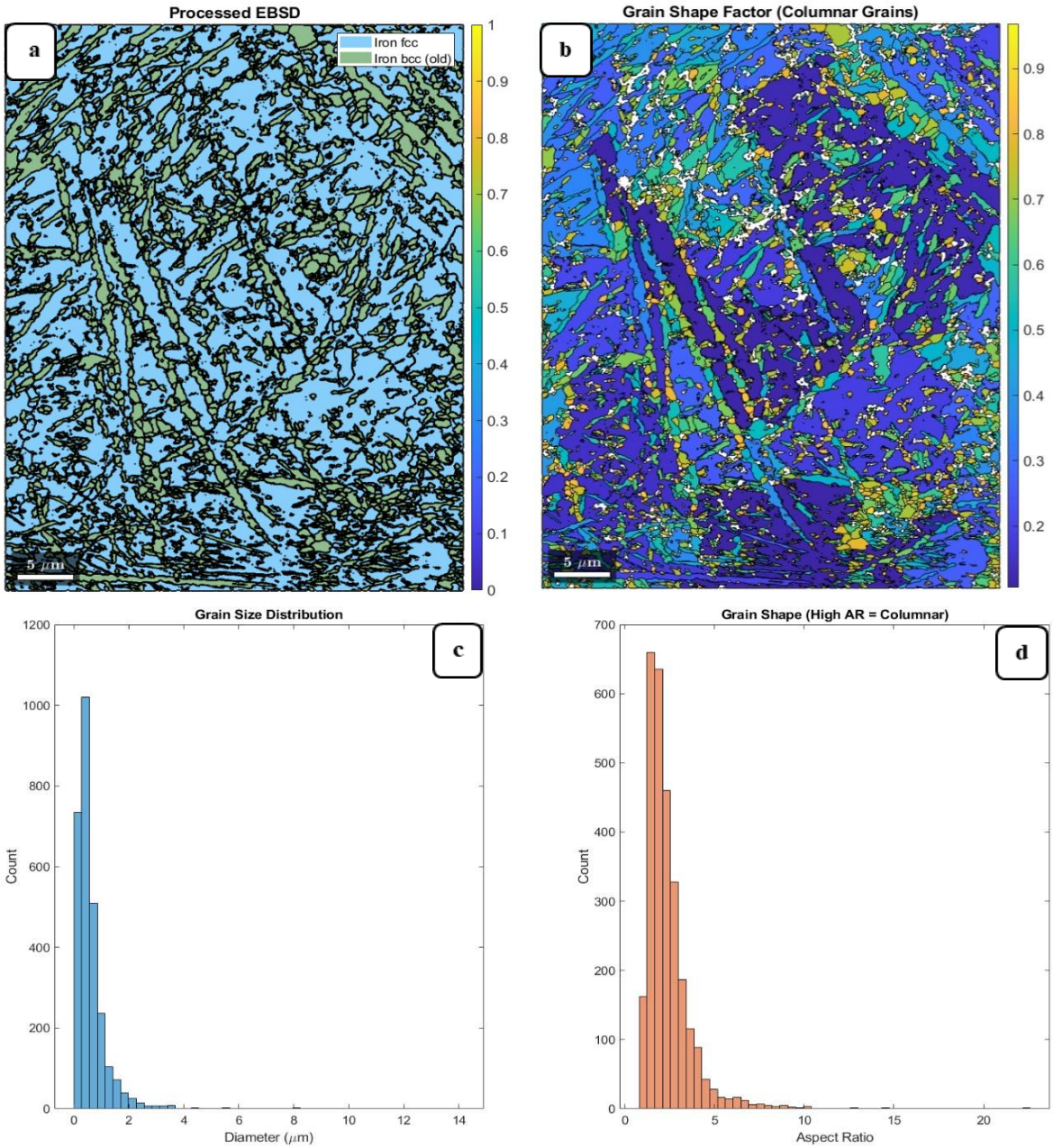


Fig. 9 Phase fraction map (a), grain shape factor map (b), grain size distribution histogram (c) and grain shape histogram (d) of the EBSD data analysed in MTEX.

Fig. 10a shows the inverse pole figure (IPF) maps, which resemble the hierarchical microstructure of an as-printed M2 HSS. This IPF map shows elongated, needle-like features that depict directional growth, such as martensite or bainite laths, and a fragmented region that reveals a fine microstructure formed during rapid solidification. The color distribution of these maps is mostly red to orange, which qualitatively indicates a strong preferred direction of crystallographic development. This texture development refers to the directed solidification during the PBF-LB/M process, which is controlled by thermal gradients. Fig. 10b provides the pole figures (PF), which give a 3D representation in 2D stereographic projections of the printed M2 HSS, and Figs. 10c and 10d are the IPF counter maps. In the pole figures (100), the red

spot (highest density of directional data) is shifted from the centre, indicating that the solidification path follows the melt pool's curved path. IPF-Z density (Fig. 10c) map confirms that the red spot is toward the [101] corner with a 31.3° tilt relative to the BD. The maximum texture intensity is observed in the small black square in the IPD-Z max density (Fig. 10d), confirming the exact orientation point. The maximum texture density (MRD) is 10.21, indicating highly organised internal grains with a mean grain size of ~0.8 µm.

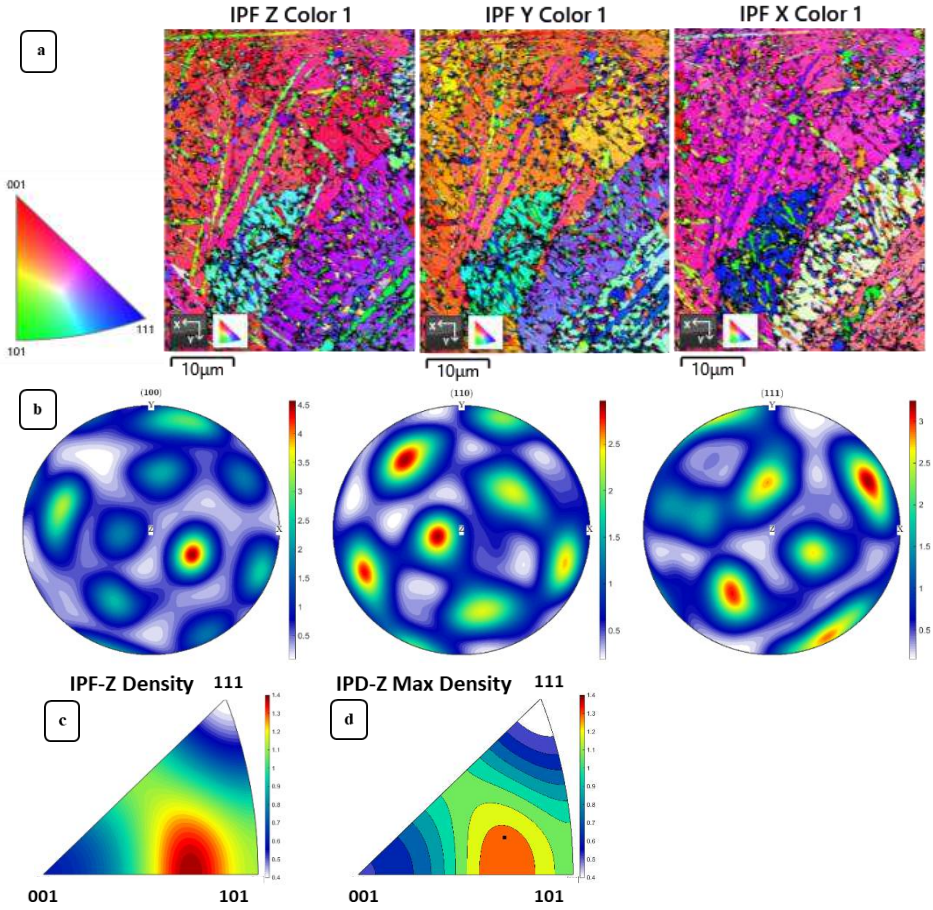


Fig. 10 Inverse pole figure (IPF) maps (a) showing lath morphology, Pole figures/density plots (b-d) showing quantitative texture analysis

4. Conclusions

The main findings of the present study are summarized as follows:

1. Repeated nested cross-validation was used to assess six regression techniques: Bayesian Ridge, RF, GBR, SVR, GPR, and quadratic RSM. RF had the best hardness prediction ($R^2 = 0.592 \pm 0.078$, MAE = 14.37 ± 1.79 HV) for the key processing parameters, while GBR had the greatest relative density prediction ($R^2 = 0.619 \pm 0.048$, MAE = 0.0438 ± 0.0032 percentage points).
2. The most important processing parameter for both hardness and relative density was found to be hatch spacing. 60 µm was chosen for experimental validation after ML-guided investigation of a narrowed hatch-spacing range of 55–70 µm.
3. A relative density of 99.94 – 99.99 % and a hardness of around 718–782 HV were obtained by reducing the hatch spacing to 60 µm. Without baseplate preheating, increased melt-track overlap enhanced consolidation and reduced the delamination seen at greater hatch spacings.
4. The as-built microstructure included equiaxed, columnar, dendritic, and refined lath morphologies along with around 50.3 % retained austenite (fcc) and about 24 % bcc phase. Grain-boundary strengthening contributed to the high hardness, with an average grain size of about 0.8 µm.
5. A strong crystallographic texture with a maximum intensity of 10.21 MRD and a preferred orientation slanted roughly 31.3° from the build direction toward [101] was found by EBSD, indicating the impact of melt-pool solidification conditions and directional heat gradients.

Overall, the study shows that PBF-LB/M parameter selection for crack-sensitive M2 HSS can be successfully guided by ML-assisted sensitivity analysis and targeted experimental verification, with 60 µm hatch spacing offering improved densification, hardness, and build integrity without baseplate preheating.

References

[1] X.F. Zhou, F. Fang, J.Q. Jiang, A Study on the Microstructure of AISI M2 High Speed Steel Manufactured by Continuous Casting, AMR 146–147 (2010) 1211–1215. https://doi.org/10.4028/www.scientific.net/AMR.146-147.1211.

[2] J.W. Park, H.C. Lee, S. Lee, Composition, microstructure, hardness, and wear properties of high-speed steel rolls, Metall Mater Trans A 30 (1999) 399–409. https://doi.org/10.1007/s11661-999-0329-9.

[3] A.S. Chaus, M. Bračík, M. Sahul, M. Dománková, Microstructure and properties of M2 high-speed steel cast by the gravity and vacuum investment casting, Vacuum 162 (2019) 183–198. https://doi.org/10.1016/j.vacuum.2019.01.041.

[4] M. Boccalini, H. Goldenstein, Solidification of high speed steels, International Materials Reviews 46 (2001) 92–115. https://doi.org/10.1179/095066001101528411.

[5] H.F. Fischmeister, R. Riedl, S. Karagöz, Solidification of high-speed tool steels, Metall Trans A 20 (1989) 2133–2148. https://doi.org/10.1007/BF02650299.

[6] M.M. Serna, J.L. Rossi, MC complex carbide in AISI M2 high-speed steel, Materials Letters 63 (2009) 691–693. https://doi.org/10.1016/j.matlet.2008.11.035.

[7] M. Godec, B.Š. Batič, D. Mandrino, A. Nagode, V. Leskovšek, S.D. Škapin, M. Jenko, Characterization of the carbides and the martensite phase in powder-metallurgy high-speed steel, Materials Characterization 61 (2010) 452–458. https://doi.org/10.1016/j.matchar.2010.02.003.

[8] M. Aslan, Powder metallurgy in additive manufacturing: Trends, challenges, methods, materials, and emerging applications, Powder Technology 476 (2026) 122420. https://doi.org/10.1016/j.powtec.2026.122420.

[9] Z. Zhang, L. Zhang, Z. Fan, R. Zhu, C. Li, H. Suen, X. He, X. Luo, Integrated process optimization of binder jetting for high-performance M2 high-speed steel: Printing parameters, bimodal powder design, and sintering strategies, International Journal of Refractory Metals and Hard Materials 137 (2026) 107690. https://doi.org/10.1016/j.ijrmhm.2026.107690.

[10] A. Choudhari, J. Elder, M. Mugale, S. Karki, V.B. Vukkum, R.K. Gupta, T. Borkar, Additive manufacturing of AISI M2 tool steel by binder jetting (BJ): Investigation of microstructural and mechanical properties, Journal of Manufacturing Processes 132 (2024) 686–711. https://doi.org/10.1016/j.jmapro.2024.11.008.

[11] Y. Wei, Y. Zhang, Y. Li, Y. Ren, S. Zhang, X. Zhang, X. Chu, S. Liu, Heterogeneous Distribution of Microstructure and Mechanical Properties in M2 High-Speed Steel Fabricated by Laser Powder Bed Fusion, Crystals 15 (2025) 917. https://doi.org/10.3390/cryst15110917.

[12] M. Zhang, C. Chen, L. Qin, K. Yan, G. Cheng, H. Jing, T. Zou, Laser additive manufacturing of M2 high-speed steel, Materials Science and Technology 34 (2018) 69–78. https://doi.org/10.1080/02670836.2017.1355584.

[13] Y. Wei, Y. Zhang, X. Chu, S. Yang, J. Wang, W. Jia, J. Zhu, S. Liu, Enhanced red hardness through fine carbides in M2 high-speed steel fabricated via electron beam powder bed fusion, Journal of Materials Research and Technology 36 (2025) 1562–1571. https://doi.org/10.1016/j.jmrt.2025.03.174.

[14] E.-S. Lee, W.-J. Park, K.-H. Baik, S. Ahn, Different carbide types and their effect on bend properties of a spray-formed high speed steel, Scripta Materialia 39 (1998) 1133–1138. https://doi.org/10.1016/S1359-6462(98)00270-X.

[15] Y.P. Yu, J.F. Huang, H. Cui, Y.H. Cai, J.S. Zhang, Microstructures and Thermostability of Spray Formed Nb-Containing High Speed Steel, AMR 418–420 (2011) 3–7. https://doi.org/10.4028/www.scientific.net/AMR.418-420.3.

[16] P. Kjeldsteen, Development of high alloyed tool steels using spray forming on an industrial scale, Powder Metallurgy 46 (2003) 297–298. https://doi.org/10.1179/pom.2003.46.4.297.
[17] Y.Q. Yang, S. Jiang, X. Zhao, Microstructure Evolution of Laser Direct Metal Deposition of M2 High Speed Steel, MSF 879 (2016) 2198–2203. https://doi.org/10.4028/www.scientific.net/MSF.879.2198.
[18] A. Jammal, G. Wang, Z. JiaXin, H. Yang, S. Yang, Y. Zhong, Y. Rong, Multi-scale modelling of solidification and microstructure evolution in laser-deposition of T15 high speed steel, Journal of Manufacturing Processes 50 (2020) 24–33. https://doi.org/10.1016/j.jmapro.2019.12.024.
[19] N. Ur Rahman, L. Capuano, S. Cabeza, M. Feinaeugle, A. Garcia-Junceda, M.B. De Rooij, D.T.A. Matthews, G. Walmag, I. Gibson, G.R.B.E. Römer, Directed energy deposition and characterization of high-carbon high speed steels, Additive Manufacturing 30 (2019) 100838. https://doi.org/10.1016/j.addma.2019.100838.
[20] N.U. Rahman, L. Capuano, M.B.D. Rooij, D.T.A. Matthews, A. Garcia-Junceda, M.A. Mekicha, L. Cordova, G. Walmag, M. Sinnaeve, G.R.B.E. Römer, Laser metal deposition of vanadium-rich high speed steel: Microstructural and high temperature wear characterization, Surface and Coatings Technology 364 (2019) 115–126. https://doi.org/10.1016/j.surfcoat.2019.02.044.
[21] J.P. Oliveira, A.D. LaLonde, J. Ma, Processing parameters in laser powder bed fusion metal additive manufacturing, Materials & Design 193 (2020) 108762. https://doi.org/10.1016/j.matdes.2020.108762.
[22] J. Saewe, C. Gayer, A. Vogelpoth, J.H. Schleifenbaum, Feasability Investigation for Laser Powder Bed Fusion of High-Speed Steel AISI M50 with Base Preheating System, Berg Huettenmaenn Monatsh 164 (2019) 101–107. https://doi.org/10.1007/s00501-019-0828-y.
[23] J. Jin, R. Gao, H. Peng, H. Guo, S. Gong, B. Chen, Rapid Solidification Microstructure and Carbide Precipitation Behavior in Electron Beam Melted High-Speed Steel, Metall Mater Trans A 51 (2020) 2411–2429. https://doi.org/10.1007/s11661-020-05661-z.
[24] T. DebRoy, H.L. Wei, J.S. Zuback, T. Mukherjee, J.W. Elmer, J.O. Milewski, A.M. Beese, A. Wilson-Heid, A. De, W. Zhang, Additive manufacturing of metallic components – Process, structure and properties, Progress in Materials Science 92 (2018) 112–224. https://doi.org/10.1016/j.pmatsci.2017.10.001.
[25] J. Xiang, H. Yang, C. Zhuang, Effect of Cooling Rate on the Characteristics of Eutectic Carbides in M2Al High-Speed Steel, Crystals 15 (2025) 493. https://doi.org/10.3390/cryst15060493.
[26] T. DebRoy, H.L. Wei, J.S. Zuback, T. Mukherjee, J.W. Elmer, J.O. Milewski, A.M. Beese, A. Wilson-Heid, A. De, W. Zhang, Additive manufacturing of metallic components – Process, structure and properties, Progress in Materials Science 92 (2018) 112–224. https://doi.org/10.1016/j.pmatsci.2017.10.001.
[27] G. Zimmermann, C. Pickmann, M. Hamacher, E. Schaberger-Zimmermann, H. Neumann-Heyme, K. Eckert, S. Eckert, Fragmentation-driven grain refinement in directional solidification of AlCu10wt-% alloy at low pulling speeds, Acta Materialia 126 (2017) 236–250. https://doi.org/10.1016/j.actamat.2016.12.063.
[28] M. Wan, W.-H. Zhang, Y. Yang, Phase width analysis of cutting forces considering bottom edge cutting and cutter runout calibration in flat end milling of titanium alloy, Journal of Materials Processing Technology 211 (2011) 1852–1863. https://doi.org/10.1016/j.jmatprotec.2011.06.008.
[29] S. Gorsse, C. Hutchinson, M. Gouné, R. Banerjee, Additive manufacturing of metals: a brief review of the characteristic microstructures and properties of steels, Ti-6Al-4V and

high-entropy alloys, Science and Technology of Advanced Materials 18 (2017) 584–610. https://doi.org/10.1080/14686996.2017.1361305.
[30] K. Kempen, B. Vrancken, S. Buls, L. Thijs, J. Van Humbeeck, J.-P. Kruth, Selective Laser Melting of Crack-Free High Density M2 High Speed Steel Parts by Baseplate Preheating, Journal of Manufacturing Science and Engineering 136 (2014) 061026. https://doi.org/10.1115/1.4028513.
[31] P. Mercelis, J. Kruth, Residual stresses in selective laser sintering and selective laser melting, Rapid Prototyping Journal 12 (2006) 254–265. https://doi.org/10.1108/13552540610707013.
[32] T. DebRoy, H.L. Wei, J.S. Zuback, T. Mukherjee, J.W. Elmer, J.O. Milewski, A.M. Beese, A. Wilson-Heid, A. De, W. Zhang, Additive manufacturing of metallic components – Process, structure and properties, Progress in Materials Science 92 (2018) 112–224. https://doi.org/10.1016/j.pmatsci.2017.10.001.
[33] R. Mertens, B. Vrancken, N. Holmstock, Y. Kinds, J.-P. Kruth, J. Van Humbeeck, Influence of Powder Bed Preheating on Microstructure and Mechanical Properties of H13 Tool Steel SLM Parts, Physics Procedia 83 (2016) 882–890. https://doi.org/10.1016/j.phpro.2016.08.092.
[34] D. Simson, C.P. Paul, S.K. Subbu, Experimental study and neural network model based prediction of layer thickness influence on LPBF IN625 single track geometry, Optics & Laser Technology 173 (2024) 110543. https://doi.org/10.1016/j.optlastec.2024.110543.
[35] J. Galarza, J. Barron, L. Jimenez, T. Oraby, J. Li, F. Ahmed, A machine learning approach to detect pores in laser powder bed fusion additive manufacturing, Manufacturing Letters 44 (2025) 985–993. https://doi.org/10.1016/j.mfglet.2025.06.117.
[36] D. Chernyavsky, D.Y. Kononenko, J.K. Hufenbach, J. Van Den Brink, K. Kosiba, Bayesian optimization for laser powder bed fusion of defect-free AA2024, Additive Manufacturing 114 (2025) 105022. https://doi.org/10.1016/j.addma.2025.105022.
[37] D.J.C. MacKay, Bayesian Interpolation, Neural Computation 4 (1992) 415–447. https://doi.org/10.1162/neco.1992.4.3.415.
[38] J. Liao, A new Bayesian lasso and ridge regression with a practically meaningful parameterization and a simple weakly informative prior, Stat 12 (2023) e540. https://doi.org/10.1002/sta4.540.
[39] A. Bedoui, N.A. Lazar, Bayesian empirical likelihood for ridge and lasso regressions, Computational Statistics & Data Analysis 145 (2020) 106917. https://doi.org/10.1016/j.csda.2020.106917.
[40] C.E. Rasmussen, C.K.I. Williams, Gaussian Processes for Machine Learning, The MIT Press, 2005. https://doi.org/10.7551/mitpress/3206.001.0001.
[41] J. Snoek, H. Larochelle, R.P. Adams, Practical Bayesian Optimization of Machine Learning Algorithms, (2012). https://doi.org/10.48550/ARXIV.1206.2944.
[42] K.P. Murphy, Machine learning: a probabilistic perspective, 4. print. (fixed many typos), MIT Press, Cambridge, Mass., 2013.
[43] S. Sellamanickam, S.K. Selvaraj, Predictive Approaches For Gaussian Process Classifier Model Selection, (2012). https://doi.org/10.48550/ARXIV.1206.6038.
[44] M. Awad, R. Khanna, Support Vector Regression, in: Efficient Learning Machines, Apress, Berkeley, CA, 2015: pp. 67–80. https://doi.org/10.1007/978-1-4302-5990-9_4.
[45] A.J. Smola, B. Schölkopf, A tutorial on support vector regression, Statistics and Computing 14 (2004) 199–222. https://doi.org/10.1023/B:STCO.0000035301.49549.88.
[46] L. Breiman, Random Forests, Machine Learning 45 (2001) 5–32. https://doi.org/10.1023/A:1010933404324.
[47] T. Chen, C. Guestrin, XGBoost: A Scalable Tree Boosting System, in: Proceedings of the 22nd ACM SIGKDD International Conference on Knowledge Discovery and Data

Mining, ACM, San Francisco California USA, 2016: pp. 785–794. https://doi.org/10.1145/2939672.2939785.
[48] J.H. Friedman, Greedy function approximation: A gradient boosting machine., Ann. Statist. 29 (2001). https://doi.org/10.1214/aos/1013203451.
[49] G.H. Golub, M. Heath, G. Wahba, Generalized Cross-Validation as a Method for Choosing a Good Ridge Parameter, Technometrics 21 (1979) 215–223. https://doi.org/10.1080/00401706.1979.10489751.
[50] A.E. Hoerl, R.W. Kennard, Ridge Regression: Biased Estimation for Nonorthogonal Problems, Technometrics 12 (1970) 55–67. https://doi.org/10.1080/00401706.1970.10488634.
[51] R.H. Myers, A.I. Khuri, W.H. Carter, Response Surface Methodology: 1966–l988, Technometrics 31 (1989) 137–157. https://doi.org/10.1080/00401706.1989.10488509.
[52] D.M. Steinberg, R.S. Kenett, Response Surface Methodology, in: R.S. Kenett, N.T. Longford, W.W. Piegorsch, F. Ruggeri (Eds.), Wiley StatsRef: Statistics Reference Online, 1st ed., Wiley, 2014. https://doi.org/10.1002/9781118445112.stat04105.
[53] B. Mondal, T. Mukherjee, T. DebRoy, Crack free metal printing using physics informed machine learning, Acta Materialia 226 (2022) 117612. https://doi.org/10.1016/j.actamat.2021.117612.
[54] Y. Du, T. Mukherjee, T. DebRoy, Physics-informed machine learning and mechanistic modeling of additive manufacturing to reduce defects, Applied Materials Today 24 (2021) 101123. https://doi.org/10.1016/j.apmt.2021.101123.
[55] J. Platl, S. Bodner, C. Hofer, A. Landefeld, H. Leitner, C. Turk, M.-A. Nielsen, A.G. Demir, B. Previtali, J. Keckes, R. Schnitzer, Cracking mechanism in a laser powder bed fused cold-work tool steel: The role of residual stresses, microstructure and local elemental concentrations, Acta Materialia 225 (2022) 117570. https://doi.org/10.1016/j.actamat.2021.117570.
[56] M.M. Monjez, N. Omidi, P. Farhadipour, N. Barka, A.E. Ouafi, Process-structure–property relationships in laser powder bed fusion of H13 tool steel: effect of processing and tempering conditions on microstructure and mechanical properties, Int J Adv Manuf Technol 139 (2025) 2481–2504. https://doi.org/10.1007/s00170-025-16024-6.
[57] M. Kaess, M. Werz, S. Weihe, Residual stress formation mechanisms in laser powder bed fusion : a numerical evaluation, (2023). https://doi.org/10.18419/OPUS-12970.
[58] J. A Ilemobayo, O. Durodola, O. Alade, O. J Awotunde, A. T Olanrewaju, O. Falana, A. Ogungbire, A. Osinuga, D. Ogunbiyi, A. Ifeanyi, I. E Odezuligbo, O. E Edu, Hyperparameter Tuning in Machine Learning: A Comprehensive Review, J. Eng. Res. Rep. 26 (2024) 388–395. https://doi.org/10.9734/jerr/2024/v26i61188.
[59] R.G. Mantovani, A.L.D. Rossi, E. Alcobaça, J. Vanschoren, A.C.P.L.F. De Carvalho, A meta-learning recommender system for hyperparameter tuning: Predicting when tuning improves SVM classifiers, Information Sciences 501 (2019) 193–221. https://doi.org/10.1016/j.ins.2019.06.005.
[60] P. Schratz, J. Muenchow, E. Iturritxa, J. Richter, A. Brenning, Hyperparameter tuning and performance assessment of statistical and machine-learning algorithms using spatial data, Ecological Modelling 406 (2019) 109–120. https://doi.org/10.1016/j.ecolmodel.2019.06.002.
[61] W. Zhao, H. Xiang, W. Chaochao, C. Huangfu, Y. Lu, Tuning hatch distance to optimize microstructure and mechanical properties of 2205 duplex stainless steel produced by laser powder bed fusion, Optics & Laser Technology 172 (2024) 110536. https://doi.org/10.1016/j.optlastec.2023.110536.
[62] A.C.D.F. Silveira, L.T. Belkacemi, P.J. De Castro, M. Schowalter, R. Fechte-Heinen, J. Epp, Effect of intrinsic heat treatment on the precipitate formation of X40CrMoV5–1

tool steel during laser-directed energy deposition: A coupled study of atom probe tomography and in situ synchrotron X-ray diffraction, Acta Materialia 283 (2025) 120488. https://doi.org/10.1016/j.actamat.2024.120488.
[63] F. Deirmina, N. Peghini, B. AlMangour, D. Grzesiak, M. Pellizzari, Heat treatment and properties of a hot work tool steel fabricated by additive manufacturing, Materials Science and Engineering: A 753 (2019) 109–121. https://doi.org/10.1016/j.msea.2019.03.027.
[64] J. Yan, H. Song, Y. Dong, W.-M. Quach, M. Yan, High strength (~2000 MPa) or highly ductile (~11%) additively manufactured H13 by tempering at different conditions, Materials Science and Engineering: A 773 (2020) 138845. https://doi.org/10.1016/j.msea.2019.138845.
[65] B. Song, X. Zhao, S. Li, C. Han, Q. Wei, S. Wen, J. Liu, Y. Shi, Differences in microstructure and properties between selective laser melting and traditional manufacturing for fabrication of metal parts: A review, Front. Mech. Eng. 10 (2015) 111–125. https://doi.org/10.1007/s11465-015-0341-2.
[66] J. Saewe, N. Carstensen, P. Kürnsteiner, E.A. Jägle, J.H. Schleifenbaum, Influence of increased carbon content on the processability of high-speed steel HS6-5-3-8 by laser powder bed fusion, Additive Manufacturing 46 (2021) 102125. https://doi.org/10.1016/j.addma.2021.102125.
[67] Y. Wang, B. Mao, S. Chu, S. Chen, H. Xing, H. Zhao, S. Wang, Y. Wang, J. Zhang, B. Sun, Advanced manufacturing of high-speed steels: A critical review of the process design, microstructural evolution, and engineering performance, Journal of Materials Research and Technology 24 (2023) 8198–8240. https://doi.org/10.1016/j.jmrt.2023.04.269.
[68] F. Maresca, V.G. Kouznetsova, M.G.D. Geers, On the role of interlath retained austenite in the deformation of lath martensite, Modelling Simul. Mater. Sci. Eng. 22 (2014) 045011. https://doi.org/10.1088/0965-0393/22/4/045011.

Statements and Declarations

Funding

This work was supported by the German Academic Exchange Service (DAAD) through a research scholarship awarded.

Competing Interests

The authors declare that they have no known competing financial interests or personal relationships that could have influenced the work, data analysis, or algorithmic outcomes reported in this paper.

Ethical Approval

This article does not contain any studies involving human participants or animal subjects performed by any of the authors. The research constitutes entirely independent, non-hazardous laboratory processing of tool steel alloys and computational data science modeling.

Data Availability Statement

All experimental input variables (laser power, scanning speed, and hatch distance) and corresponding material property outputs (relative density and bulk hardness) required to replicate the machine-learning benchmarking, predictive pipelines, and sensitivity calculations are fully embedded and disclosed in this article.

Author Contributions

S.K.S. performed the experimental work, data analysis, machine-learning modeling, microstructural characterization, visualization, and interpretation of the results, and wrote the original manuscript. A.U. supervision, interpretation of the results, and critical revision of the manuscript. F.O. contributed to the PBF-LB/M experiments, interpretation of the results, and review of the manuscript. U.K. supervision, interpretation of the results, and critical review and editing of the manuscript. All authors reviewed and approved the final manuscript.

Supplementary Files

This is a list of supplementary files associated with this preprint. Click to download.

- GraphicalAbstract.pdf
- Highlights.docx